Dynamics of excess electron migration, solvation, and spectra in polar molecular clusters

R. N. Barnett and Uzi Landman
School of Physics, Georgia Institute of Technology, Atlanta, Georgia 30332

Abraham Nitzan
School of Chemistry, Sackler Faculty of Science, Tel Aviv University, 69978, Tel Aviv, Israel

The dynamics of excess electron localization, migration, and solvation in water and ammonia clusters, and the time-resolved spectroscopic consequences of these processes, are investigated via computer simulations. In these simulations, the solvent evolves classically and the electron propagates in the ground state. The coupling between the polar molecular cluster and the electron is evaluated via the quantum expectation value of the electron–molecule interaction potential. Starting from an electron attached to a cold molecular cluster in a diffuse weakly bound surface state, temporal stages of the electron solvation and migration processes, leading to the formation of an internally solvated state, and the associated variations in the excitation spectra are described. The migration of the excess electron during the penetration is characterized by a nonhopping, polaronlike mechanism.

I. INTRODUCTION

The mechanisms and dynamics of electron solvation and migration in fluids are key issues in advancing our understanding of a number of important chemical and physical phenomena such as carrier mobility, electron transfer reactions,[1] electrochemical processes and chemical reactions in solution,[2] electron solvation in fluids[3–8] and electron attachment and localization in clusters.[9]

Recent developments of theoretical methods for simulations of quantum-mechanical dynamical evolution[3,10–23] in condensed phase systems open new avenues for investigations of these phenomena on refined temporal and spatial scales. Furthermore, the emerging availability of ultrafast time-resolved spectroscopic data on such systems[2,6] provides an added impetus for enhanced theoretical efforts.

In this paper, we focus on investigations of the dynamics of electron penetration and localization in water and ammonia clusters. While electron solvation in bulk[5,24,25] liquid ammonia and water as well as in small clusters[26] have been studied for quite a while, experimental[27–32] and theoretical[9,10,12,13,24,33–38] studies of electron attachment and localization in small clusters of these materials have been recently the focus of intensive investigations. On the experimental side, it has been found that while single water and ammonia molecules do not attach an electron readily (if at all), negatively charged water[27,28,30–32] $(H_2O)_n^-$, and ammonia[29] $(NH_3)_m^-$ clusters have been prepared either by localization during the cluster nucleation process[27–31] (for both water and ammonia), or via capture of very low energy electrons by cold water clusters.[32] These clusters were detected for $n \geqslant 11$ and $m \geqslant 30$, respectively, and accurate values of the vertical binding energies for $(H_2O)_n^-$, clusters for $(11 \leqslant n \leqslant 30)$ have been obtained via photoelectron spectroscopy.[31] Recent theoretical investigations employing the quantum path-integral molecular dynamics (QUPID) method[9,24,33–36] and time-dependent SCF (TDSCF) simulations[10,12] revealed that electron localization in $(H_2O)_n^-$, clusters occurs via two modes, depending on the cluster size; surface (i.e. exterior) states for $8 < n \lesssim 64$ and a gradual transition to internal localization which develops fully for $n \gtrsim 64$. In contrast, ammonia clusters[36] of any size do not support well-bound excess electron surface states, resulting in the onset of electron binding via internal localization for $n \gtrsim 32$, in agreement with experimental observations.[29]

While the above studies addressed the energetics and structure of excess electron localization in clusters, the path-integral simulations are not suited for investigations of real-time evolution. To study the time evolution of an excess electron interacting with a cluster, we have employed methods in which the real-time dynamical development of the coupled electron–cluster system is simulated.[9–13,38] In conjunction with classical dynamics of the atomic constituents coupled to the excess electron via the expectation value (with respect to the electronic wavefunction) of the interaction between the electron and the atoms [i.e., the time-dependent self-consistent-field method (TDSCF)], two modes of dynamical simulations have been used:

(i) Simulations in which the time evolution of the electron is obtained via a numerical solution of the time-dependent Schrödinger equation[3,9–16,22,38–43] (where the time dependence enters via the classical dynamics of the atomic constituents which are coupled to the electron).

(ii) An Adiabatic Simulation Method[3,9–13,38] (ASM), where the electron is constrained to remain in a given state and is described by a wave function which corresponds to the instantaneous (dynamical) nuclear configuration. In the case where the chosen electronic state is the ground state (as in the calculations in this paper), we term this mode of simulation as Ground State Dynamics (GSD). This method is applicable when there is a separation of time scales between the motion of the electron and the classical subsystem so that the latter evolves adiabatically on a single electronic potential energy surface (the Born–Oppenheimer approximation). The method, when used appropriately, i.e., within the validity of the Born–Oppenheimer approximation which implies that other electronic states do not play a significant

dynamical role, allows efficient investigations of the detailed dynamical mechanisms of electron localization, penetration, and solvation with refined temporal and spatial resolution.

In our simulations, we start from a system in which an excess electron is initially attached to an equilibrated neutral cluster in the ground electronic state [a $(H_2O)_{256}^-$, cluster at 300 K and two cluster sizes $(NH_3)_{64}^-$ and $(NH_3)_{256}^-$ at 189 K have been investiaged]. The GSD simulations of the negatively charged clusters are carried out at constant energy. As shown below (see Sec. III), the average kinetic temperatures of the classical degrees of freedom in the negatively charged clusters do not change significantly throughout the simulation. In the initial state, the electron is weakly bound to the molecular cluster in a diffuse surface state. The initial time evolution ($t \lesssim 0.15$–0.3 ps) is characterized by a reorientation of the cluster environment concomitant with an increase in the magnitude of the ground-state energy of the excess electron, an increase in the separation between the ground and first excited states, and a transition to a compact wave function. While at the very beginning of this initial stage the assumptions underlying the GSD method are not fully satisfied, subsequent time evolution is described faithfully by this method. Following the initial stage, we identify three dynamical stages (depending slightly on the molecular cluster size).

(i) 0.15–$0.3 \lesssim t \lesssim 3$–$4$ ps for the ammonia clusters and $0.15 < t < 1.2$ ps for water; during this stage the excess electron explores various sites on the surface of the cluster accompanied by local cluster reorganization in the vicinity of the electron, and culminating in the formation of a well-bound surface state.

(ii) 3–$4 < t < 4$–5 ps for ammonia and $1.2 < t < 1.5$ ps for water; during this fast stage, the first molecular solvation shell is formed and sudden (in less than 1 ps) increases occur in the magnitudes of the electronic ground state energy and separation between the ground and excited states, achieving values characteristic of the fully solvated electron.

(iii) $t > 4.5$ ps for ammonia and $t > 1.5$ ps for water; in this stage, migration of the electron towards the center of the cluster occurs, characterized by gradual buildup of successive solvation shells, and "polaronlike" dynamical evolution where the electron-induced cluster reorganization accompanies the migration of the electron.

The main issues concerning the dynamics of excess electrons in polar fluids are the mechanisms of localization, trapping and solvation, and the spectroscopic consequences of these processes.[3,6–8,10] With regard to the initial stage of localization of an excess electron in polar fluids, contributions due to both preexisting trapping sites[6–8,44–48] as well as charge-induced polarization[49–51] have been considered. Considerable experimental and theoretical evidence has been advanced that both processes may contribute. Most recently, it was concluded from theoretical investigations[46] based on calculations of excess electron states for representative solvent configurations generated via classical molecular dynamics at 283 K, that upon the introduction of an excess electron into pure liquid water, and prior to any induced liquid configurational relaxation, the electron can be physically localized in a distribution of shallow ground states and

that under these circumstances localized excited states are rare. Moreover, recent experiments,[6] in which the time evolution of the optical absorption spectrum of excess electrons in water was studied at the femtosecond time scale, have shown an initial rise of a broad infrared absorption with a characteristic time scale of $\lesssim 110$ fs, which can be assigned as originating from shallow initial ground-state trapping, or from an excited state of the excess electron. Following this stage, a coincident disappearance of the initial state and a relaxation into the fully solvated state was observed with a characteristic time scale of 240 fs. Furthermore, the absence of spectral shift during the time evolution between these two stages of solvation had been noted, and it was tentatively suggested[6] that the second stage may correspond to an electronic transition, perhaps mediated by the dielectric relaxation of the medium.

In this study, our focus is on the dynamics of excess electrons in finite polar molecular clusters. These systems introduce new aspects in relation to studies of excess electron in bulk fluid systems, such as the inherent inhomogeneity of the system (i.e., surface and interior cluster environments), the distinction between surface and interior modes of electron localization,[9,10,24,34–37] and the process of penetration[10] (when the internal localization mode is thermodynamically favorable). Nevertheless, it is worthwhile to note that the separation of dynamical stages which we find for these systems (particularly the sudden transition from a shallow bound state to an almost fully solvated state, and the corresponding sudden change in the excitation spectrum) and the time scales on which they occur, are reminiscent of the temporal stages and their spectral manifestations discussed in the context of time-resolved spectroscopy of electron localization and solvation in bulk fluids.[6]

In Sec. II, a review of the GSD simulation method is given, including details of the implementation of the method for our studies. Results for the dynamics and energetics of electron localization, solvation and penetration, and a discussion of the mode of migration in $(H_2O)_{256}^-$, $(NH_3)_{64}^-$ and $(NH_3)_{256}^-$ clusters are given in Sec. III.

II. METHOD

A. The Adiabatic Simulation Method (ASM)

As mentioned in the Introduction, while it is possible to implement the time-dependent self-consisten-field (TDSCF) formulation for studies of real-time dynamics of a quantum subsystem coupled to dynamical classical degrees of freedom, in our present investigations we limit ourselves to the adiabatic time evolution of such a coupled quantum-classical system (i.e., excess electron interacting with a classical polar cluster). This adiabatic simulation method[9–15,38] [ASM and its ground state dynamics (GSD) version] affords a significant reduction in computational time for processes which are essentially adiabatic as compared to the full real-time dynamical evolution. Clearly the method is suited for situations where th subsystems comprising the system are characterized by widely separated time scales, such as the situations normally treated by the adiabatic or Born–Oppenheimer approximation. In fact, by construction the

method is a numerical implementation of the adiabatic approximation where the electron (fast subsystem) is assumed (and is constrained) to remain at all times in a specified eigenstate of the Hamiltonian corresponding to the instantaneous configuration of the classical particles (the slow subsystem). Thus, denoting by $\{\mathbf{R}_i(t)\}$ the collection of coordinates of the classical particles, the Hamiltonian for the excess electron can be written as

$$\hat{H}(t) = \hat{K} + \hat{V}(\{\mathbf{R}_i(t)\}), \qquad (1)$$

where $\hat{K}$ and $\hat{V}$ are the kinetic and potential energy operators. The eigenstates of this Hamiltonian are the solutions to the Schrödinger equation

$$\hat{H}(t)|\psi_l(\{\mathbf{R}_i(t)\})\rangle = E_l(t)|\psi_l(\{\mathbf{R}_i(t)\})\rangle, \quad l = 0,1,2,\ldots . \qquad (2)$$

In the mixed quantum classical version of the TDSCF approximation (TDSCF), the dynamical evolution of the classical particles obeys Newton's equations

$$M_j\ddot{\mathbf{R}}_j = \mathbf{F}_j - \nabla_{\mathbf{R}_j}U(\{\mathbf{R}_i\}), \quad j = 1,\ldots,N_c, \qquad (3)$$

where N_c is the number of classical particles, $U(\{\mathbf{R}_i\})$ is the interparticle interaction potential, and the force $\mathbf{F}_j$ is evaluated via the Hellmann–Feynman theorem

$$\mathbf{F}_j = -\int d\mathbf{r}\, \psi_l^*(\mathbf{r};\{\mathbf{R}_i(t)\}[\nabla_{\mathbf{R}_j}V(\mathbf{r},\{\mathbf{R}_i(t)\})]$$
$$\times \psi_l(\mathbf{r},\{\mathbf{R}_i(t)\}), \qquad (4)$$

where the integration is over the electronic coordinates and V is the interaction potential between the electron and the atomic constituents.

The desired state $|\psi_l(t)\rangle$ (where the explicit dependence on $\{R_j\}$ has been dropped) can be obtained from an arbitrary state $|\psi\rangle$ [assuming that the two are not orthogonal, i.e., $\langle\psi_l(t)|\psi\rangle \neq 0$] by the operation[21b]

$$\lim_{\beta\to\infty} e^{-\beta\hat{H}(t)}\hat{P}_l(t)|\psi\rangle \to \langle\psi_l(t)|\psi\rangle e^{-\beta E_l(t)}|\psi_l(t)\rangle, \qquad (5)$$

where the projection operator $\hat{P}_l(t)$ is given by

$$\hat{P}_l(t) = 1 - \sum_{m=0}^{l-1}|\psi_m(t)\rangle\langle\psi_m(t)| \quad (l\neq 0), \qquad (6)$$

and $\hat{P}_0(t) \equiv 1$ for the ground state ($l = 0$, which is the case in GSD). As seen from Eq. (5), determination of an excited state l, requires the prior determination of all the lower energy eigenstates. Note also that the operation in Eq. (5) can be regarded as evolution of the wave function in imaginary time $t = -i\hbar\beta$. This fact is conveniently used in converting the computer programs from performing real-time evolution of the wave function to the operation described by Eq. (5).

The above equations define the Adiabatic Simulation Method (ASM). The numerical implementation of the operation on the left-hand side of Eq. (5) is achieved by the split-operator fast-Fourier transform (FFT) method.[20–22] First, denoting $|\bar{\psi}\rangle_l = \hat{P}_l(t)|\psi\rangle$, the left-hand side of Eq. (5) can be written as

$$e^{-\beta\hat{H}}|\bar{\psi}\rangle_l = \lim_{J\to\infty}\prod_{J=1}^{J}(e^{-\beta\hat{K}/2J}e^{-\beta\hat{V}/J}e^{-\beta\hat{K}/2J})|\bar{\psi}\rangle_l. \qquad (7)$$

Evaluation of the right-hand side of Eq. (7) proceeds by performing the $\hat{K}$ and $\hat{V}$ operations in the momentum and

coordinate spaces, respectively (since the kinetic energy operator is diagonal in the momentum representation and the potential energy operator is diagonal in the coordinate representation). At this stage, the wave function and potential are defined on a grid with periodic boundary conditions and the FFT method is used to switch between the coordinate and momentum representations of the wave function.[22] In these calculations, an error proportional to $\Delta\beta^3$, where $\Delta\beta = \beta/J$ is introduced due to the noncommutativity of the kinetic and potential energy operators. Also, in practical applications, the projection operator (6) is performed several times during the imaginary time evolution [Eq. (7)] in order to avoid the growth of lower states amplitudes due to numerical errors. In addition, we note that the grid representation, introduced in connection with the FFT, restricts the spatial resolution (determined by the mesh size) and the momentum (and thus the kinetic energy) range which can be described.[20]

B. Application to finite systems

The introduction of the grid representation for the wave function and the interaction potential between the quantum particle and the atoms $V(\mathbf{r},\{\mathbf{R}_i\})$ implies a spatial periodicity of these quantities determined by the dimensions of the grid. In order to use the method for studies of a finite system (or in general for systems characterized by nonperiodic potentials) and in particular in studies of localized ground-state properties, one must assure that the amplitude of the wave function under study as well as the amplitudes of wave functions corresponding to lower energy eigenvalues vanish at the surface of the grid. These conditions can be satisfied for any localized state by simply assuring that the spatial extent of the employed grid is large enough. This can be accomplished by either increasing the number of grid points or by increasing the grid spacing. However, an increase in the number of grid points results in increased computation time, while increasing the grid spacing decreases the spatial resolution and (consequently) the energy range that can be accounted for.

In the problem we wish to study, the temporal evolution of a molecular cluster with an attached electron (in the ground state), the excess electron density $\rho(\mathbf{r})$ is localized, but its spatial extent and position may change in time. To facilitate the application of the FFT-GSD method to this problem, we have devloped an efficient "moving grid" algorithm in which the position and spatial extent of the density are monitored and the grid is adjusted accordingly. The algorithm is outlined below:

(i) At time t we have the positions and velocities of the atomic constituents of the molecular cluster $\{\mathbf{R}_i(t)\}$ and $\{\dot{\mathbf{R}}_i(t)\}$ and the ground state wave function $\psi(\mathbf{r},t) \equiv \psi_0(\mathbf{r};\{\mathbf{R}_i(t)\})$ defined only at the grid points. The grid point positions are denoted by $\mathbf{r}_{lmn} = \mathbf{r}_0 + (l,m,n)\Delta$, where Δ is the grid spacing and $\mathbf{r}_0$ is the vector defining the origin of the grid. The amplitude of the wave function at the grid points is $\psi_{lmn}(t)$ and the wave function is normalized, i.e., $\Sigma_{l,m,n}\,\psi_{lmn}^*(t)\psi_{lmn}(t) = \Delta^{-3}$.

(ii) Compute the center-of-density

$$\mathbf{r}_e = \Delta^3 \sum_{l,m,n} \mathbf{r}_{lmn} \psi^*_{lmn} \psi_{lmn} \qquad (8)$$

and the density weighted grid surface-to-volume ratio

$$\gamma = 1 - \Delta^3 \sum_{l,m,n = -N/2+2}^{N/2-1} \psi^*_{lmn} \psi_{lmn}. \qquad (9)$$

(a) If γ is larger than a cut-off value γ_{max} {chosen as 2.5% of the uniformly weighted grid surface to volume ratio which for a cubic grid containing N^3 points is given by $[N^3 - (N-2)^3]/N^3$}, then the simulation is stopped and is restarted with either a larger N or Δ. Conversely, when $\gamma \ll \gamma_{max}$, it is beneficial to decrease Δ and/or N.

(b) If any component of $\mathbf{r}_e - \mathbf{r}_0$ is larger in magnitude than Δ, the grid is moved by one grid spacing in the appropriate direction and the new grid points (i.e., on the surface of the grid) are assigned zero wave function amplitudes.

(iii) Compute the electron–cluster interaction potential at the grid points $V(\mathbf{r}_{lmn})$ and the derivatives with respect to nuclear coordinates $\partial V(\mathbf{r}_{lmn})/\partial \mathbf{R}_i$. The potential felt by the electron at time $t + \Delta t$ is estimated by

$$V(t + \Delta t, \mathbf{r}_{lmn}) \simeq V(t, \mathbf{r}_{lmn})$$
$$+ \sum_{i=1}^{N_c} [\partial V(t, \mathbf{r}_{lmn})/\partial \mathbf{R}_i] \cdot \dot{\mathbf{R}}_i \Delta t. \qquad (10)$$

The forces on the nuclei resulting from the elctron–molecule interaction are obtained from Eq.(4).

(iv) The wave function at the grid points is updated to $\psi_{lmn}(t + \Delta t)$ using Eqs. (5) and (7) [with $\psi_{lmn}(t)$ in place of the arbitrary function ψ] and using the estimated potential $V(t + \Delta t, \mathbf{r}_{lmn})$.

(v) The intra- and intermolecular potential and forces are computed and the nuclear positions and forces are evolved to time $t + \Delta t$ using Eq. (3).

Note that the use of the estimated interaction potential $V(t + \Delta t)$ [Eq. (10)] allows us to eliminate a separate loop over grid points and molecules. Another alternative would be to compute the forces on the nuclei at time t from $\psi_0(t - \Delta t)$, but this requires a much smaller time increment

Δt in order to conserve the total energy over a lengthy simulation. The "moving grid" part of the algorithm (step ii) allows us to use a smaller grid spacing (Δ) and/or number of grid points (N^3). The values of the various parameters and other details of the simulations are given in Table I.

In our simulations, the interaction between the electron and the ground state ammonia molecules was described via a pseudopotential, constructed in the spirit of the density functional method and consisting of Coulomb, polarization, exclusion, and exchange contributions.[24,35] This interaction potential was developed and used by us previously in extensive Quantum Path-Integral Molecular Dynamics (QUPID) studies of electron solvation in water and ammonia clusters.[9,24,34–37] For the intermolecular interactions in ammonia, we have employed the potential proposed by Hinchliffe et al.[52] (model C), and for the intramolecular interactions, we used a harmonic valence-coordinate model potential based on the one discussed by Herzberg.[53,54] The RWK2-M potential[55] was used for water.

III. RESULTS

A. Temporal evolution, energetics, and structure

Simulations for ammonia clusters of two sizes [$(NH_3)^-_{64}$ and $(NH_3)^-_{256}$] at 189 K and for $(H_2O)^-_{256}$ at 300 K were performed (in the figures, results are shown for the larger clusters only). In each case, we start with a phase-space configuration of the neutral molecular cluster (nuclear positions and momenta) selected at random from the canonical equilibrium ensemble at the desired temperature. Using the FFT method, the ground state of an excess electron attached to the selected neutral cluster configuration (with the nuclear positions kept frozen) is obtained. In all cases, the so-obtained initial ground state is characterized by a diffuse excess electron density distribution with low binding energy [$E_0 = -0.003$ and -0.011 hartrees for $(NH_3)^-_{64}$ and $(NH_3)^-_{256}$, respectively, and -0.008 hartrees for $(H_2O)^-_{256}$, for the particular initial configurations used in

TABLE I. Details of the simulations. Columns 3 and 4 give the number of grid points N along an edge and the grid spacing Δ for the grid representation of the excess electron wave function. The parameters J and β (columns 5 and 6) refer to Eq. (7) and the succeeding paragraph. The last column ΔE_{total} gives the difference between the minimum and maximum of the total energy of the systems and indicates the degree to which energy was conserved during the time interval. Energy and distance in atomic units (hartree and bohr radius, respectively).

System	Time interval (ps)	N	$\Delta(a_0)$	J	β(1/a.u.)	ΔE_{total} (a.u.)
$(NH_3)^-_{64}$	0.0–0.263 5	32	3.0	100	0.023 34	0.003
	0.263 5–5.797	16	3.0	100	0.023 34	0.002
	5.797–10.276	16	1.5	50	0.011 67	0.003
$(NH_3)^-_{256}$	0.0–0.115 94	32	2.0	100	0.023 34	0.003
	0.115 94–0.168 64	32	2.0	50	0.011 67	0.001
	0.168 64–4.426 8	16	2.0	50	0.011 67	0.021
	4.426 8–10.645 4	16	1.5	50	0.011 67	0.004
	10.645 4–18.550	16	1.5	33	0.007 702 2	0.010
$(H_2O)^-_{256}$	0–0.092 2	32	1.5	100	0.023 34	0.001
	0.092 2–0.508 6	32	1.5	50	0.011 67	0.004
	0.508 6–1.470	16	2.0	50	0.011 67	0.004
	1.470–5.036	16	1.5	25	0.005 84	0.015
	5.036–22.70	16	1.5	50	0.011 67	0.012

the present simulations]. Having prepared the initial state in this manner, the nuclear coordinates are allowed to evolve in time (starting with the initial selected velocities) and the excess electron ground-state wave function corresponding to the instantaneous nuclear coordinates is reevaluated after each integration time step of the nuclear coordinates' equations of motion. Throughout the simulations, the total energy of the system remains constant.

The time evolution of the excess electron ground-state energy (E_0) and its kinetic (K) and potential (V) components are shown in Figs. 1(a) and 2(a) for the $(H_2O)_{256}^-$ and $(NH_3)_{256}^-$ clusters, respectively. The distance of the center of the excess electron density (r_e) from the molecular cluster center-of-mass (r_{cm}) and the width $r_g = \langle \psi_0 | (r - r_e)^2 | \psi_0 \rangle^{1/2}$ of the ground-state electron density distribution are shown in Figs. 1(b) and 2(b). In addition, we show in Figs. 1(a) and 2(a) the values of the first three excited states, at selected times during the evolution (denoted by dots). Four temporal stages of the systems' evolution can be discerned from these figures.

Stage 1: $t = 0$–0.15 ps (for $n = 256$ for both water and ammonia); $t = 0$–0.3 ps [for $(NH_3)_{64}^-$].

This stage is characterized mainly by the initial reorganization of the cluster in response to the presence of the electron, exhibited by reorientation of the molecules resulting in a decrease in magnitude of the intermolecluar interaction potential energy $\phi^{(2)}$ [see Fig. 3(a) for water] and an in-
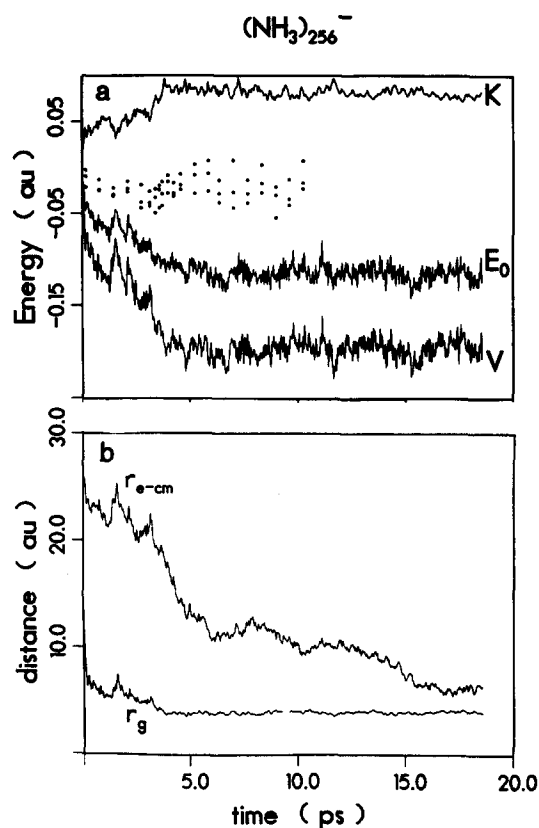
(NH₃)₂₅₆⁻

FIG. 2. The same as Fig. 1, for an excess electron in a $(NH_3)_{256}^-$ cluster at $T = 189$ K, in the time range $0 \leqslant t \leqslant 19$ ps.

(H₂O)₂₅₆⁻
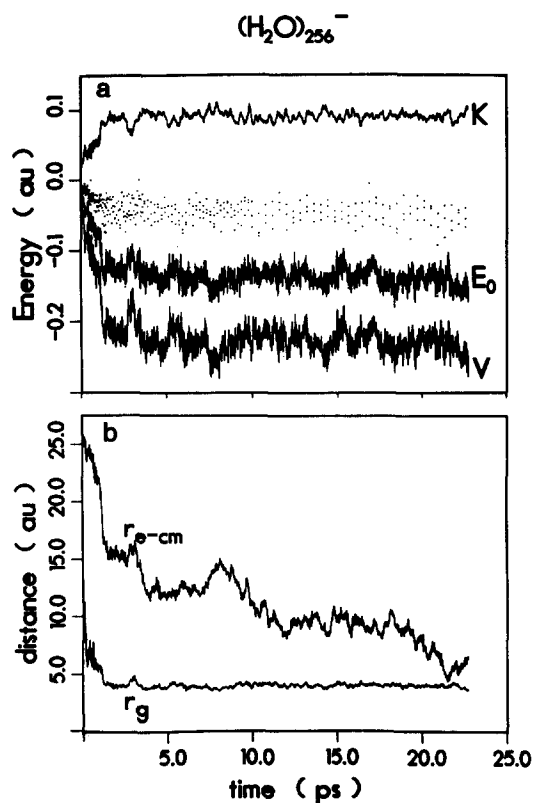

FIG. 1. Time evolution of an excess electron in a $(H_2O)_{256}^-$ cluster at $T = 300$ K. (a) The electron ground state energy E_0 and the potential V and kinetic K energy contributions for $0 \leqslant t \leqslant 23.0$ ps. The first three excited states are given at selected times by the dots. (b) Width of the electron distribution r_g and distance of the center of the excess electron distribution from the cluster center-of-mass $r_{e\text{-}cm}$ vs time. Energies and distances are in atomic units (hartree and bohr radius) and time is in ps.
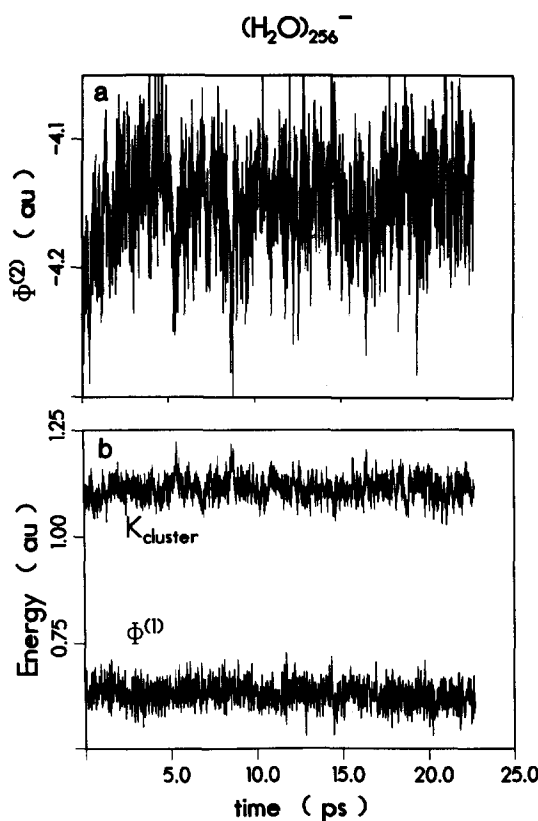
(H₂O)₂₅₆⁻

FIG. 3. Time evolution of molecular energies in $(H_2O)_{256}^-$. (a) Intermolecular potential energy $\Phi^{(2)}$. (b) Intramolecular potential energy $\Phi^{(1)}$ and kinetic energy of the molecules $K_{cluster}$. Energies are in atomic units.

crease in the dipole moment of the cluster. Coupled to the cluster reorganization is an increase in the magnitude of E_0 [the excess electron ground-state energy, e.g., from -0.011 hartree at $t = 0$ to -0.045 hartree at $t = 0.15$ ps for $(NH_3)_{256}$, and from -0.008 at $t = 0$ to -0.03 hartree at 0.15 ps for water], a decrease in the width of the wave function (see $r_g = \langle \psi_0 | (\mathbf{r} - \mathbf{r}_e)^2 | \psi_0 \rangle^{1/2}$ in Figs. 1(b) and 2(b),

and an increase in the separation between the electronic ground and first excited states[56] [$\Delta E_1 = E_1 - E_0$, see Figs. 1(a) and 2(a)]. Thus, while at the beginning of the simulations the conditions under which the ground-state dynamics (GSD) method is valid (i.e., the adiabatic approximation) are not fully satisfied, towards the end of stage 1 the use of the GSD method is fully justified.
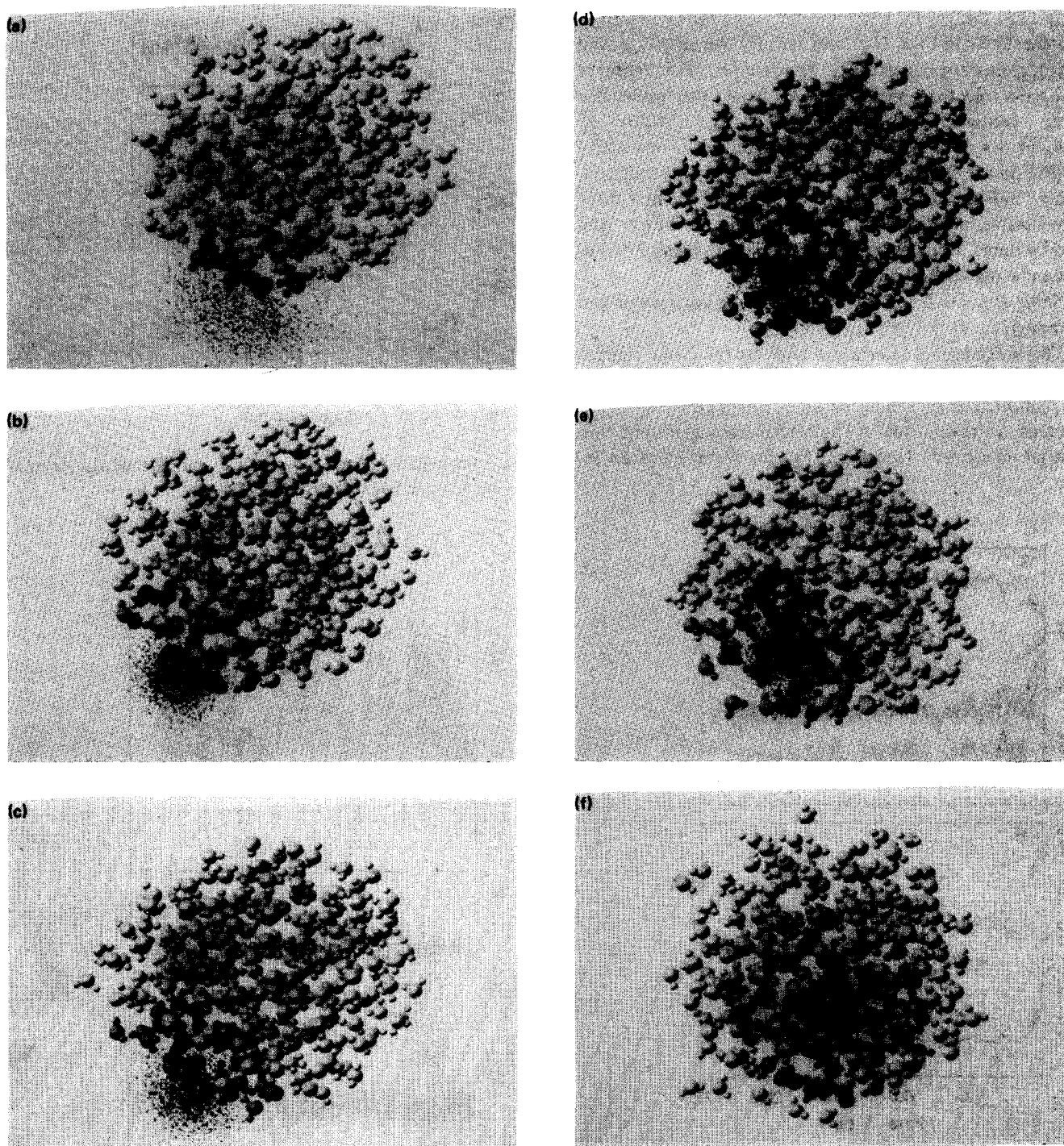

FIG. 4. Snapshots of molecular configurations and excess electron distribution (small dots) during the evolution of $(H_2O)_{256}^-$. For similar snapshots for $(NH_3)_{256}^-$, see Ref. 10. (a) $t = 0$ exhibiting a diffuse electron distribution; (b) $t = 0.25$ ps, demonstrating transition to a compact, localized surface state; (c) $t = 0.99$ ps demonstrating the initial stage of the solvation process; (d) $t = 1.5$ ps, illustrating penetration and formation of the first solvation shell; (e) $t = 5$ ps, illustrating configuration during migration; (f) $t = 21$ ps, configuration toward the end of the process, illustrating a fully solvated electron in an interior cavity in the cluster. The graded shades of the water molecules denote molecular shells. From darkest to lightest: $s1a(0, 7.0\,a_0)$, $s1b(7.0, 10.0\,a_0)$, $s2(10.0, 15\,a_0)$, and $(15\,a_0, \infty)$.

To substantiate this conclusion, concerning the validity of the GSD method, we have followed the *real-time evolution*, without the ground-state constraint, of the $n = 256$ systems within the Time-Dependent Self-Consistent-Field (TDSCF) approximation starting at $t = 0$ and at $t = 0.168$ ps for ammonia, and starting at $t = 0.225$ ps for water. When the adiabatic approximation holds the two method, namely GSD and real-time TDSCF propagation, would yield identical results. We found that the electronic and intermolecular potential ($\phi^{(2)}$) energies calculated by the two methods starting at $t = 0.168$ ps for ammonia and for all $t > 0.225$ ps for water are essentially identical for the entire time spans. In the GSD method, the electron is forced to remain in its ground–state (corresponding to the instantaneous nuclear configuration) while in the real-time TDSCF method the wave function may acquire components other than the ground state. Therefore, the fact that both simulations yield the same results validates our assertion that at this time the adiabatic approximation, and thus the use of the GSD method, is justified. On the other hand, at the very initial stage only an approximate agreement between the results obtained via the two methods is found.

Snapshots of the molecular cluster configurations and electron density distributions for $(H_2O)_{256}^-$ at $t = 0$ and $t = 0.25$ ps are shown in Figs. 4(a) and 4(b), respectively. Corresponding snapshots for the $(NH_3)_{256}^-$ cluster can be found in Ref. 10.

Stage 2: 0.15 ps $\leqslant t \leqslant 1.2$ ps for $(H_2O)_{256}^-$; 0.15 ps $\leqslant t \leqslant 3$ ps for $(NH_3)_{256}^-$; 0.3 ps $\leqslant t \leqslant 4$ ps for $(NH_3)_{256}^-$.

During this stage the excess electron remains bound in a surface state and explores various sites on the surface of the cluster. Accompanying the motion of the electron is a significant increase in the magnitude of E_0, a gradual variation in the excitation spectrum (shown for water in Fig. 5), and a significant reorganization of the molecular cluster, mainly in the vicinity of the electron, evidenced by the further increase of the intermolecular potential energy ($\phi^{(2)}$), shown in Fig. 3(a) for water, and of the magnitude of the cluster dipole
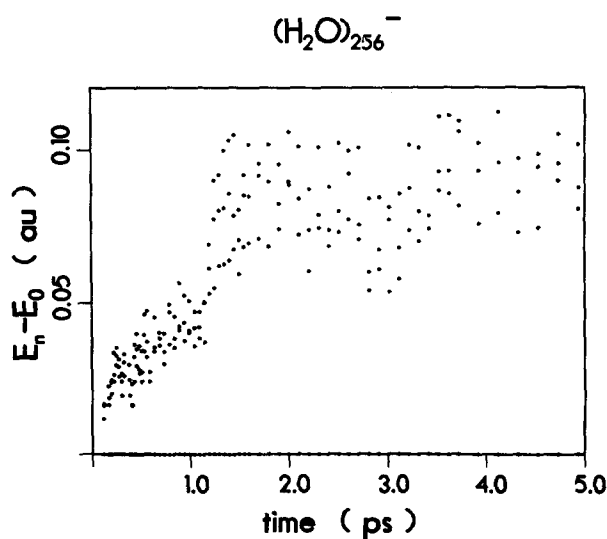
moment. Note that the increase in $\langle \phi^{(2)} \rangle$ is approximately equal to the increase in magnitude of the excess electron energy E_0, while the intramolecular potential energy $\langle \phi^{(1)} \rangle$ and the kinetic energy of the atomic constitutents (K_{cluster}) are fluctuating about a constant value (see Fig. 3).

While during this stage the electron is confined mainly to the outer region of the cluster, the initial stage of the electron solvation process begins as evidenced by an increase in the number of near-neighbor molecules [see Fig. 6(a) for water]. In this figure, the number of molecules in a sphere of radius $10\ a_0$ centered on r_e (shell $s1$), and a decomposition into subshells [0–$7.0\ a_0$ ($s1a$) and 7.0–$10\ a_0$ ($s1b$)] are shown (the choice of these shell radii is guided by the radial distribution of the molecules around the fully solvated electron, see below). The major increase in the number of neighboring molecules is in the outer range of 7.0–$10\ a_0$ [shell $s1b$ in Fig. 6(a)].
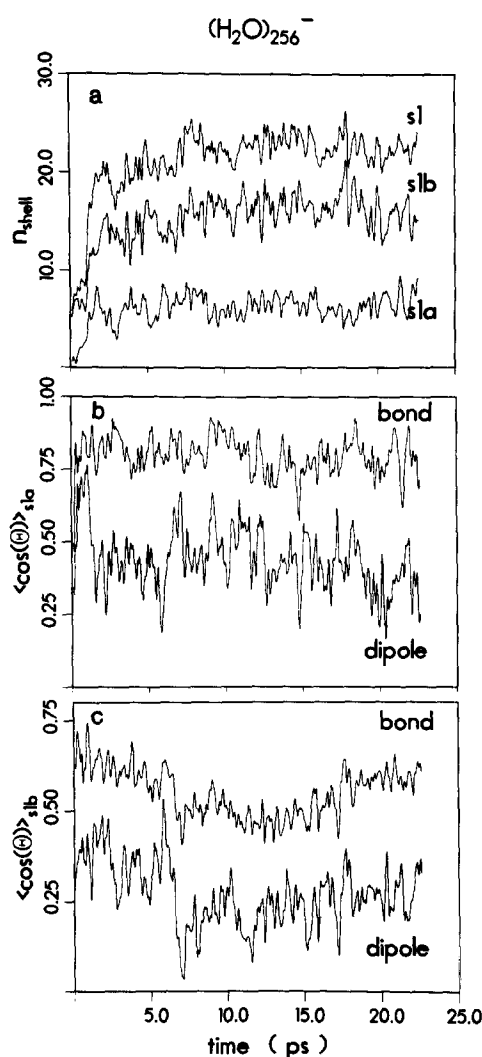

$(H_2O)_{256}^-$

FIG. 6. (a) The number of water molecules n vs time in the first shell ($s1$) around the center of the excess electron density r_e. Shell $s1$ is defined in the range $(0, 10\ a_0)$; subshells $s1a$ and $s1b$ in the intervals $(0, 7.0\ a_0)$ and $(7.0, 10\ a_0)$, respectively. The choice of shells is guided by the molecular distribution about the fully solvated electron. (b) and (c) Time variation of the cosine of the angle between $r_e - r_0$ and the water molecular dipoles, and between $r_e - r_0$ and the bond vector $r_H - r_0$ forming the minimum angle with respect to the former vector, in subshells $s1a$ and $s1b$. For a random distribution of the molecular orientations $\langle \cos(\theta_{\text{bond}}) \rangle = 0.3954$ and $\langle \cos(\theta_{\text{dipole}}) \rangle = 0$.

$(H_2O)_{256}^-$

FIG. 5. The excitation spectrum $E_n - E_0$, $n = 1$–3, of an excess electron in $(H_2O)_{256}^-$, for $0 \leqslant t \leqslant 5$ ps. No significant variation occurs beyond the time span shown. Note the sharp increase in the excitation spectrum at $t \approx 1.2$ ps.

In addition to the radial distribution of molecules, the local environment of the electron can be characterized by the orientation of the molecules with respect to the center r_e of the excess electron density. In Figs. 6(b) and 6(c), plots of $\langle\cos(\theta_{bond})\rangle$ and $\langle\cos\theta_{dipole}\rangle$ are shown for water molecules in shells $s1a$ and $s1b$, where

$$\cos(\theta_{bond}) = \max\left[\frac{(\mathbf{r}_e - \mathbf{r}_O)\cdot(\mathbf{r}_H - \mathbf{r}_O)}{|\mathbf{r}_e - \mathbf{r}_O||\mathbf{r}_H - \mathbf{r}_O|}\right] \quad (11a)$$

and

$$\cos\theta_{dipole} = \frac{(\mathbf{r}_e-\mathbf{r}_O)\cdot\mu}{|\mathbf{r}_e - \mathbf{r}_O||\mu|}, \quad (11b)$$

where $\mathbf{r}_O$ is the location of the oxygen atom in a water molecule and $\mathbf{r}_H$ is the location of that hydrogen atom of the molecule whose O–H bond forms the minimum angle with respect to $\mathbf{r}_e - \mathbf{r}_O$. μ is the dipole moment of the molecule and the angular brackets indicate averages over the molecules within the radial shells. For a random distribution of the molecular orientations in water,

$$\langle\cos(\theta_{bond})\rangle = \frac{1}{\pi}\int_0^\pi d\theta \sin\theta \int_0^{\pi/2} d\phi[\sin\alpha\sin\theta\cos\phi$$
$$+ \cos\alpha\cos\theta] = 0.3954, \quad (12)$$

where $\alpha = 52.27°$ is the angle between the O–H bond and the symmetry axis of H_2O molecule, and $\langle\cos(\theta_{dipole})\rangle = 0$. From Figs. 6(b) and 6(c), we observe that following the increase in both $\langle\cos(\theta_{bond})\rangle$ and $\langle\cos(\theta_{dipole})\rangle$ in stage 1, they fluctuate about values which correspond to a high degree of bond orientation (i.e., O–H and N–H bonds, in the water and ammonia clusters, respectively, pointing to the center of the excess electron density) for molecules within 7.0 a_0 (7.5 a_0 for ammonia) from the electron as well as preferred dipole orientation for the neighboring molecules. For both systems, this ordering is considerable also in the second subshell [$s1b$, see Fig. 6(c)]. To investigate the spatial range over which orientational ordering occurs, the number of molecules in more distant shells (10–15 a_0, $s2$; and 15–25 a_0, $s3$) as well as $\langle\cos\theta_{dipole}\rangle$ and the interaction potential between the excess electron and the molecules are given in Fig. 7 for water. The dipole orientation parameter $\langle\cos(\theta_{dipole})\rangle$ for the more distant shells, shown in Fig. 7(b), indicates less pronounced orientational ordering than in the vicinity of the electron (shell $s1$), which correlates with the smaller values of the interaction energy between molecules in those shells and the excess electron [see Fig. 7(c)]. Nevertheless, the long-range nature of the interaction should be noted.

A snapshot of the molecular cluster configuration and of the electron density distribution for $(H_2O)_{256}^-$ close to the end of stage 2 is shown in Fig. 4(c).

Stage 3: 1.2 ps $\leqslant t \leqslant$ 1.5 ps for $(H_2O)_{256}^-$; 3 ps $\leqslant t \leqslant$ 5 ps for $(NH_3)_{256}^-$; 4 ps $\leqslant t \leqslant$ 5 ps for $(NH_3)_{64}^-$.

Following the formation of a well-bound surface state during stage 2, the system evolves in a dramatic manner signified by sharp changes in energetic and structural characteristic quantities. In this stage, the first molecular solvation shell around the excess electron is completed. As seen in Fig. 6(a), the number of molecules within 7.0 a_0 (7.5 a_0 for am-
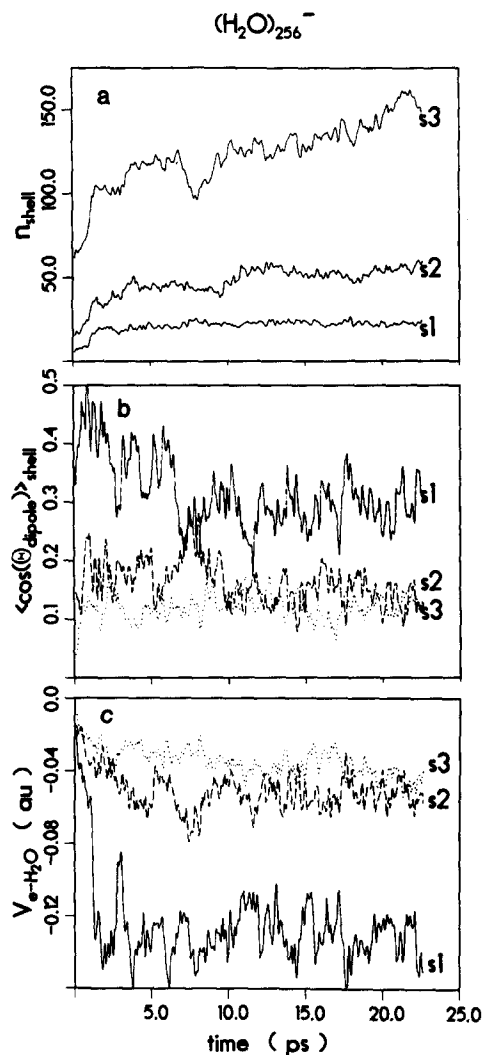
$(H_2O)_{256}^-$

FIG. 7. (a) The number of water molecules n vs time in shells around r_e; $s1$ (0,10 a_0); $s2$ (10, 15 a_0); $s3$ (15, 25 a_0). (b) The same as Fig. 6(b) for the above shells. (c) Excess electron–water interaction potential energy decomposed in shells.

monia) from r_e (subshell $s1a$) increases suddenly to about 6 (at $\sim$1.25 ps for water and at $\sim$3.3 ps for ammonia), and fluctuates about this value for the remainder of the simulation. In conjunction with the formation of the solvation cavity, the excess electron density contracts [see r_g, in Figs. 1(b) and 2(b)] and the center of density penetrates towards the center of the cluster (see $r_{e\text{-}cm}$). Note also that the formation of the first solvation shell results in a decrease in the orientational order of more distant molecules and a decrease in the total cluster dipole moment due to screening of the excess electron charge by the first solvation shell. A snapshot of the molecular configuration and electron density distribution for $(H_2O)_{256}^-$ at the end of this stage is shown in Fig. 4(d), demonstrating the formation of the first molecular solvation shell around the electron.

These structural changes are accompanied by pronounced sudden changes in the excess electron ground-state potential and kinetic energies [Figs. 1(a) and 2(a)] and excitation energies [see Fig. 5 for $(H_2O)_{256}^-$]. Note that these changes occur in less than 1 ps and correlate with the

sudden increase in the number of molecules within 7.0 a_0 (for water) and 7.5 a_0 (for ammonia) of r_e. The values of the electron ground-state energy E_0 and excitation energies at the end of this fast stage are close to those of the fully solvated electron. In this context, we note that the calculated sudden increase in the excitation energies, which would exhibit itself as a shift of the absorption spectrum to shorter wavelength, is reminiscent of the shift in the absorption spectrum from an initial absorption peaking in the infrared to an absorption maximum at the wavelength characteristic of the fully solvated electron observed in recent studies of the dynamics of excess electron solvation in liquid water following photoionization,[6] and in theoretical studies of electron solvation.[3,13,46]

Stage 4: $t > 1.5$ ps for $(H_2O)_{256}^-$; $t > 5$ ps for both $n = 64$ and 256 ammonia clusters.

Having established in stage 3 a local environment characteristic of a fully solvated electron, the systems continue to evolve with the migration of the excess electron towards the center of the cluster accompanied by gradual buildup of successive solvation shells [see Figs. 7(a) and 7(c)]. Radial distribution functions of the molecular oxygens and hydrogens about the electron center of density, towards the end of the simulations, are shown in Fig. 8 for $(H_2O)_{256}^-$ at two

temperatures and in Fig. 9 for $(NH_3)_{256}^-$ at 189 K. In addition to the results of this study, we show for the ammonia cluster (Fig. 9) comparisons to the radial distribution obtained by us in a previous[35,54] quantum-path-integral molecular-dynamics (QUPID) investigation of these clusters. We note the clearly delineated solvation shell structure and the excellent agreement between the results of the two studies. Further comparison between the results for the fully solvated electron obtained by the two methods (i.e., GSD and QUPID) is given in Table II.

Further information about the structure and energetics of the fully solvated electron in $(H_2O)_{256}^-$ is obtained from a radial plot of the excess electron potential energy shown in Fig. 10 for two temperatures. In this figure as well as in the atomic radial distribution functions (see Fig. 8), the formation of a clearly defined solvation shell structure is evident. As seen, the effect of higher temperature is to somewhat blur the distinction of solvation shells beyond the first one.

Snapshots of the water cluster configuration and the excess electron density at 5 ps and at the end of the simulation are shown in Figs. 4(e) and 4(f).

We note that the solvation shell structure and the tendency of molecules in the first solvation shell to be bond
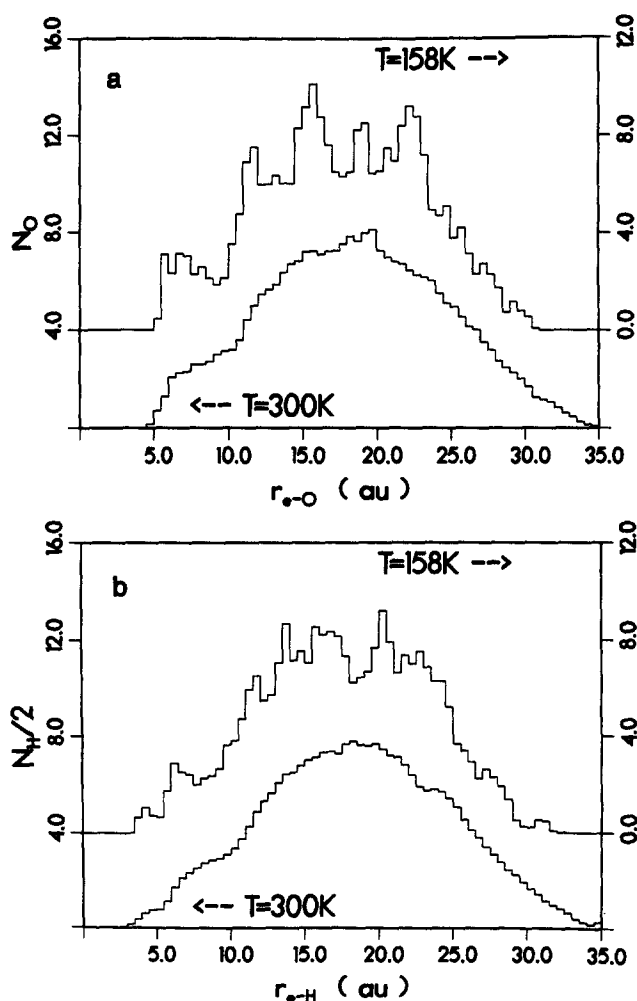
FIG. 8. Radial distribution of (a) oxygens and (b) hydrogens about the center of the excess electron density in the fully solvated state in $(H_2O)_{256}^-$, at $T = 158$ and 300 K.
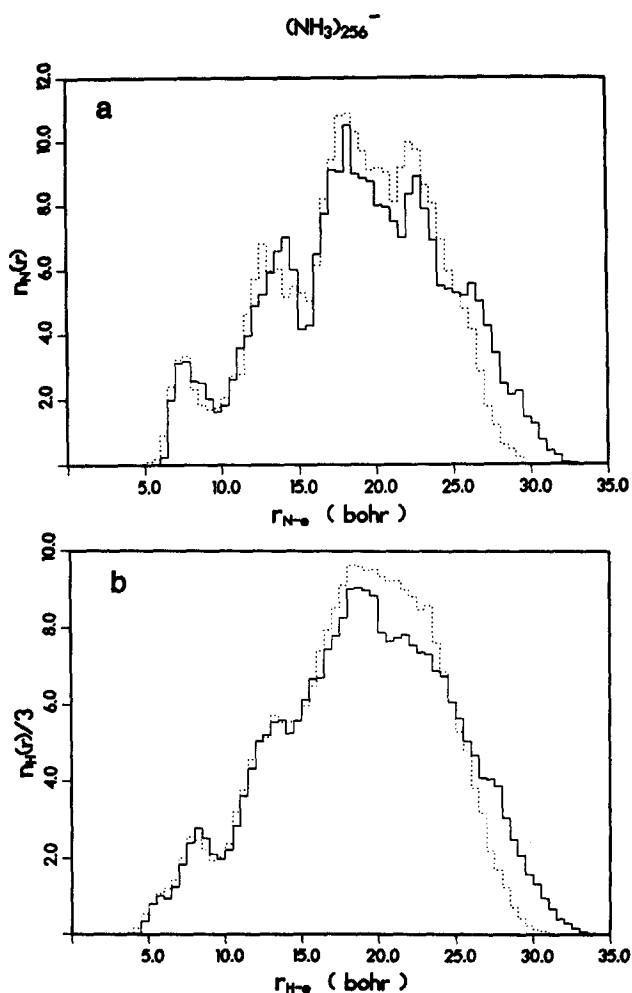
FIG. 9. Radial distributions in $(NH_3)_{256}^-$ of (a) nitrogens and (b) hydrogens about the center of the excess electron density in the fully solvated state at 189 K. Solid and dashed lines correspond to the present GSD and previous (Ref. 36) QUPID calculations, respectively.

TABLE II. Comparison between the results obtained in our calculations using the FFT-GSD method and Quantum Path-Integral Molecular-Dynamics (QUPID) simulations (Refs. 36 and 54) for $(NH_3)_n^-$ clusters ($n = 64$ and 256). The QUPID simulations (Refs. 36 and 54) were carried at constant temperature $T = 189$ K (canonical ensemble). Results are shown for the intra- and intermolecular potential energies $\langle \phi^{(1)} \rangle$ and $\langle \phi^{(2)} \rangle$, respectively; kinetic energy of the molecules $K_{cluster}$; interaction potential energy between the electron and the cluster V; kinetic energy of the electron K; the total excess electron energy $E = K + V(E = E_0$ for the FFT-GSD calculations); and width of the electron distribution r_g. Note that the cluster kinetic energy $K_{cluster}$ for $n = 64$ is higher in the GSD calculation than in the QUPID simulations, due to the velocities of the molecules in the initial neutral cluster (chosen randomly from an equilibrium canonical ensemble). This kinetic energy corresponds to a kinetic temperature of the cluster molecules of 236 K rather than 189 K used in the canonical QUPID simulations. The differences in the results of $n = 64$ between the two methods are due to that difference in temperature. Energies are in hartrees and r_g are in bohr radii.

| | $n = 64$ | | $n = 256$ | |
	GSD	QUPID	GSD	QUPID
$\langle \phi^1 \rangle$	0.1526	0.1304	0.5133	0.5201
$\langle \phi^2 \rangle$	−0.3873	−0.4569	−2.3697	−2.3735
$K_{cluster}$	0.2865	0.2304	0.9213	0.9213
V	−0.1557	−0.1729	−0.1930	−0.2008
K	0.0768	0.0812	0.0779	0.0863
E	−0.0789	−0.0917	−0.1151	−0.1145
r_g	4.17	3.87	4.01	4.01

oriented, rather than dipole oriented, towards the center of the excess electron distribution found in these simulations (as well as in our previous QUPID simulations of excess electrons internal localization in water[24] and ammonia[36] clusters) is in agreement with results obtained via simulations[57] of electron hydration in bulk water in which a different interaction potential for the interaction between water molecules, as well as between the excess electron and the molecules, was used. Furthermore, bond orientation is exhibited in our simulations already at the initial stages of the electron penetration process [see Fig. 6(b)], even before the first solvation shell is completely developed. This observa-
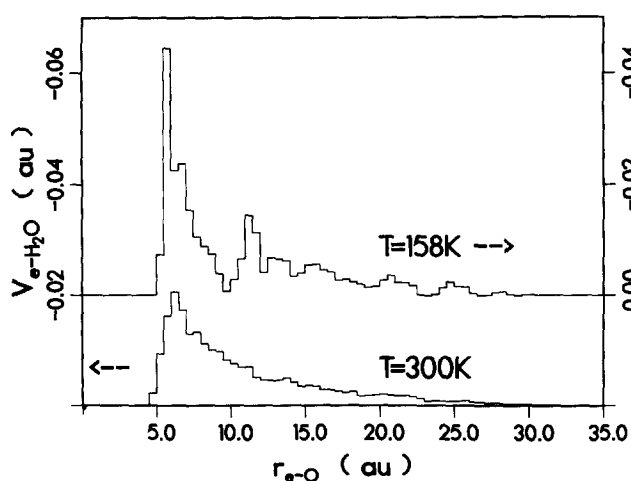

FIG. 10. Radial distribution of the excess electron–molecule interaction potential energy in $(H_2O)_{256}^-$, in the fully solvated state, at $T = 158$ and 300 K. Note the marked solvation shell, structure and the blurring of that structure, beyond the first shell at the higher temperature.

tion indicates the role of local orientational reorganization of the molecules, in the vicinity of the excess electron, in the process of localization (trapping) of the initial surface state.

The dynamical evolution and the time scales associated with the processes of electron attachment, penetration, migration, and localization in polar molecular clusters, exhibited as we have illustrated above in variations in structural, energetic, and spectroscopic properties, are consequences of the nature of interactions and response mechanisms in these systems. As discussed above, the dynamics of structural reorganization, and in particular reorientational mechanisms of the cluster molecules in response to the presence of the excess electron, play a dominant role in the temporal evolution of the system. Therefore, the quantitative significance of our results depends upon the adequacy of the interaction potentials used in our simulations. Based on our previous extensive studies of excess electron localization[9,10,24,34–38,58] and the dynamics of electron solvation[13] in water and ammonia clusters and the quantitative correspondence between the results of these studies and experimental data, we believe that the results obtained in our current investigations provide quantitative estimates of the time scales characterizing the dynamical evolution in these systems. Obviously certain quantitative details, and in particular the initial state and the first stage of the evolution of the coupled excess electron–cluster system, depend upon the particular initial configurations of the molecular clusters which were chosen at random from the corresponding equilibrium ensembles. Nevertheless, from the correspondence among the results for the three systems shown in this paper, and from additional simulations which we have performed starting from other initial cluster configurations, we conclude that the time scales of the evolution which we have observed are faithful estimates characteristic of the dynamical mechanisms of response and structural reorganization in these systems.

B. Mode of electron migration

In the above we have investigated the time evolution of the coupled electron–cluster system and have exhibited the structural and energetic temporal variations in the properties of the system as the electron solvates in an internally localized state. We turn next to a detailed investigation of the nature of the electron penetration (migration) process. This process clearly involves quantum-mechanical evolution of the electron coupled to the dynamics of the cluster environment. In fact, the molecular reorganization of the molecular cluster is essential for the evolution of the solvated state which does not develop if the cluster classical degrees of freedom are frozen in their initial state configuration.

In studying the migration of an electron in condensed media which do not possess translational periodicity (i.e., in our case, the penetration of the electron from the external surface to the interior of the cluster), several modes of propagation may be considered. Studies of excess electron migration in molten salts[14] suggest that the electron transport in these systems is mostly due to short-time jumps between two spatially separated sites. This mechanism is characterized by the occurrence of configurations, where at the intermediate time (between sites) the wave function exhibits splitting

(i.e., a bimodal electron density distribution is found), and it appears that a potential barrier separate the initial and final localized states of the electron.[14] In our simulations, we did not find evidence for such electron hopping events. In particular, we did not find configurations of the excess electron which are characterized by a bimodal distribution of the electron density distribution. Such events would have been exhibited in large variations in the width of the excess electron distribution r_g, which are absent in our results (see Figs. 1 and 2). We remark that the fact that the excess electron wave function remains localized at all times serves as a

posterior consistency check on the employment of the TDSCF method in our simulations.

To examine the mode of electron motion in our systems, we have picked a region in the cluster about which the electron is centered at a particular time [$t_r = 21$ ps for $(H_2O)_{256}^-$ and $t_r = 10.65$ ps for $(NH_3)_{256}^-$] after the start of the dynamical evolution ($t = 0$), and have monitored properties of that region starting from $t = 0$ till the end of the simulation. The region which we selected is centered with a radius of 7.0 a_0 for water and 7.5 a_0 for ammonia around the center-of-density of the electron at t_r, $\mathbf{r}_e(t_r)$. The time variation of the distance of the electron from that point $|\mathbf{r}_e(t) - \mathbf{r}_e(t = t_r)|$ is shown in Figs. 11(a) and 12(a), for water and ammonia, respectively, which demonstrate the approach and entrance
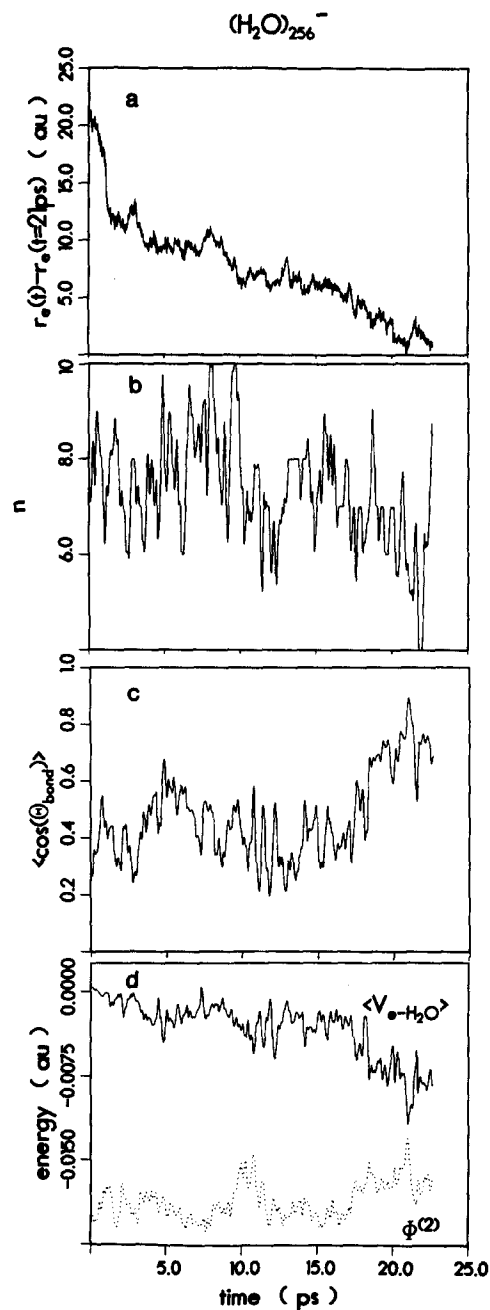

FIG. 11. The $(H_2O)_{256}^-$ cluster. (a) Distance of the center of the excess electron density at time t, $\mathbf{r}_e(t)$, from its location at $t = 21$ ps. Number of molecules n in (b); $\langle \cos(\theta_{bond}) \rangle$ in (c); per molecule electron–water molecule interaction potential energy and intermolecular interaction potential energy $\Phi^{(2)}$ (dashed line) in (d). All the quantities in (b)–(d) are calculated for molecules in a spherical region of radius 7.0 a_0 about $\mathbf{r}_e(t = 21$ ps).
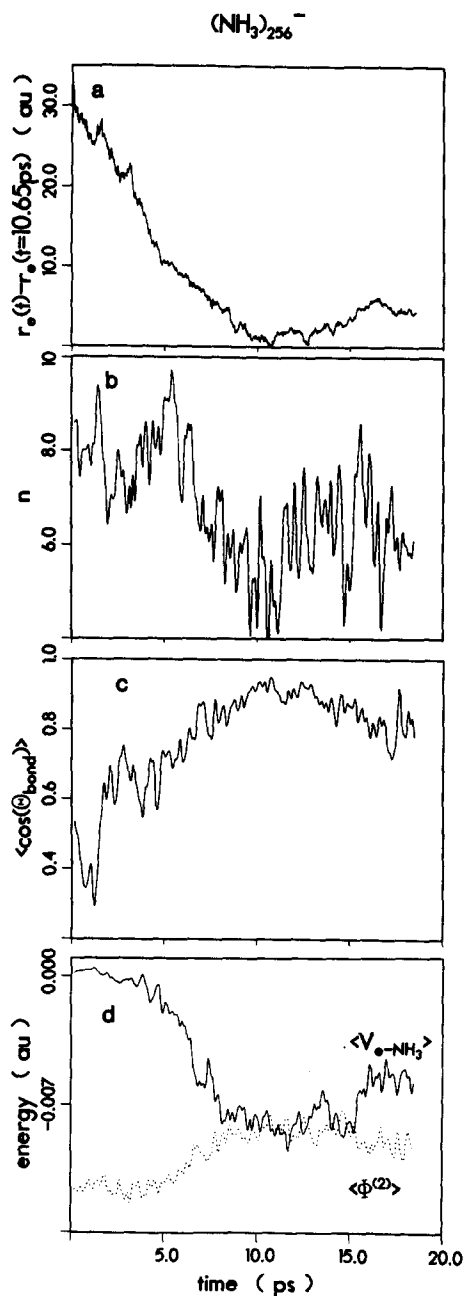
FIG. 12. The same as Fig. 11, but for the $(NH_3)_{256}^-$ cluster with reference to the center of the excess electron density at $t = 10.65$ ps and a spherical region of radius 7.5 a_0 about that location.

of the electron into the above region and its subsequent departure. In Figs. 11(b) and 12(b), the variation in time of the number of molecules residing within the specified region is shown. As seen, the penetration of the electron into the region is accompanied by a marked gradual decrease in the number of molecules in it, which is a consequence of the formation of a solvation cavity (containing the electron) centered in this region. The structural reorganization of the cluster environment in the vicinity of the solvated electron is the cause for this variation [note that in the fully solvated state, the number of H_2O or NH_3 molecules in the first coordination shell ($s1a$) is ~ 6]. The migration of the electron subsequent to reaching the specified region is accompanied by an increase in the number of molecules in the selected region {more clearly seen for the $(NH_3)_{256}^{-}$ cluster [Fig. 12(b)]}.

As we have discussed above (Figs. 6 and 7), the interaction between the electron and the molecules induces, throughout the electron propagation, a high degree of preferred orientational order (i.e., O–H or N–H bonds pointing toward the center of excess electron density) in the vicinity of the electron [within ~ 7.0 or 7.5 a_0 of $r_e(t)$ for water or ammonia, respectively]. In Figs. 11(c) and 12(c), the time variation of the bond-orientation order parameter $\langle \cos \theta_{\text{bond}} \rangle$ [see Eq. 11(a)] averaged over molecules in the selected region, is displayed. As expected from our previous discussion, the degree of bond orientation in the region increases upon the approach of the electron.

The variations in the electron–molecule interaction potential energy averaged over molecules in the selected region (solid line) and the per molecule intermolecular interaction energy (dotted line) in the region are shown in Figs. 11(d) and 12(d). The correlation between the increase in the magnitude of the electron–molecule interaction and the process of molecular reorganization as exhibited by the increase in the intermolecular potential energy is evident.

The difference between the electron migration mechanisms in molten alkali halides[14] and in our polar molecular systems may be attributed to the difference in the host reorganization energy in these systems. In the case of molten alkali halides, the solvated electron substitutes for a halide anion and the energy of the region containing the electron is close to that of neighboring regions in the fluid. On the other hand, in a polar molecular system, the energy of a region around the solvated excess electron is much larger in magnitude than that of an equivalent neighboring neutral region. Furthermore, in the latter case, due the sizeable reorganization energy[24] which accompanies the formation of the solvation shells (see Fig. 13), solvent fluctuations leading to a favorable solvation site in a neutral region are unlikely. Indeed the absence of deep traps in neutral water has been recently demonstrated.[46]

The magnitude and spatial extent of the cluster reorganization energy and electron–cluster interaction can be inferred from the variations in the intermolecular interaction potential energy $\Phi^{(2)}$ (see Fig. 3) and for the fully solvated electron in the $(H_2O)_{256}^{-}$ cluster (i.e., at the end of the simulation) from the energy radial distributions shown in Fig. 13. The solid line in this figure represents the molecular vertical
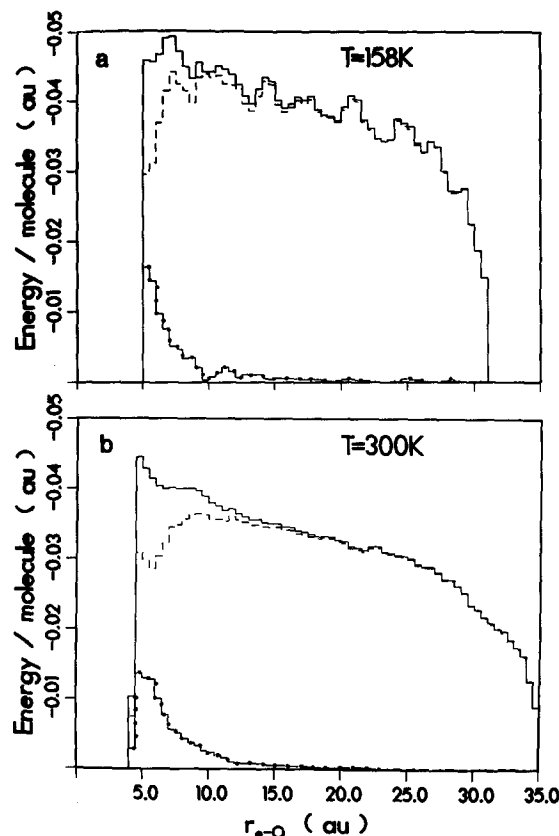

FIG. 13. The solid line represents the radial distribution of the molecular vertical binding energy (MVBE) [See Eq. (13)] of a water molecule, i.e., the negative of the average energy required to remove an H_2O molecule (whose oxygen is a distance r from the center of the fully solvated excess electron density) from the cluster, without allowing molecular or electronic relaxation, for $(H_2O)_{256}^{-}$ at (a) 158 K and (b) 300 K. The contributions to MVBE from the intermolecular interactions, i.e., excluding the electron–water interaction is represented by the dashed line. The electron–water interaction potential energy is represented by the dash–dotted line. The effect of higher temperature is to blur the distinction of solvation shells beyond the first one.

binding energy MVBE(r) defined as[24]

$$\text{MVBE}(r) = [2\Phi^{(2)}(r) + V(r)]/n_{e-0}(r), \qquad (13)$$

where $V(r)$ is the interaction energy between the excess electron whose center of density is at r_e and the $n_{e-0}(r)$ water molecules whose oxygens lie within a shell of radii r and $r + \Delta r$ about r_e. The individual contributions from $2\Phi^{(2)}(r)$ and $V(r)$ are indicated by the dashed and dashed–dotted lines, respectively. As seen from this figure the spatial extent of the electron–water interaction V and the molecular reorganization which can be obtained from $\Phi^{(2)}$ by subtracting from it its value at the center of a corresponding neutral cluster [see Fig. 9(b) in the second paper in Ref. 24 where that value for $(H_2O)_{256}$ at 300 K is $\sim - 0.037$ a.u.] is largely contained within a sphere of radius 10 a_0 about the solvated electron. For molecules in the first solvation shell $s1a$ (0,7 a_0), the reorganization energy per molecule is of the order of a hydrogen bond energy in water.

As shown by our previous QUPID calculations,[24,34–36] the adiabatic binding energy (i.e., the electron ground state

energy plus the cluster reorganization energy) of an excess electron to a polar molecular cluster favors internal localization for sufficiently large clusters [$n \gtrsim 64$ for $(H_2O)_n^-$ and $n \gtrsim 32$ for $(NH_3)_n^-$]. In addition, a continuum dielectric model for excess electrons in finite molecular aggregates[24,37] yielded results in agreement with these calculations and experimental data, and demonstrated the importance of the long-range polarization interaction in stabilizing the solvated state. As seen from Figs. 7(c) and 13, while the largest contribution to the electron potential energy comes from its interaction with the first solvation subshell, $s1a$ (0–7.0 a_0 for water and 0–7.5 a_0 for ammonia), which is fully developed at an early stage, the long-range interaction with the furthest away molecular shells and the development of these shells provide the driving force for migration from the surface to the interior where that contribution is maximized. The mechanism of migration is polaron-like in nature, with the electron propagating in a spatially localized solvated ground state via polarization of the dynamical host environment (no "dragging" of molecules accompanies the migration of the electron). The spectral consequences [i.e., the sudden increase in the excitation energy (see Fig. 5 for water)] of the time evolution of the electron–cluster system remain an experimental challenge.

Finally we note that the time scale for electron penetration from the surface into the cluster and the formation of an excess electron state exhibiting properties of an internally solvated electron is of the order of a few picoseconds [<2 ps for $(H_2O)_{256}^-$ at 300 K and ~5 ps for $(NH_3)_{64}^-$ and $(NH_3)_{256}^-$ at 189 K]. From this observation, we conclude that both methods of preparation of such negatively charged molecular clusters (i.e., electron localization during the cluster nucleation process[27-31] or via the capture of very low energy electrons by preexisting clusters[32]) would yield similar results, as long as probing of the clusters occurs past the short time required for penetration.

ACKNOWLEDGMENT

[1]See the review by G. McLendon, Acc. Chem. Res. **21**, 160 (1988) and references therein.

[2]See the review by J. D. Simon, Acc. Chem. Res. **21**, 128 (1988); M. Maroncelli, E. W. Castner, Jr., S. P. Webb, and G. R. Fleming, in *Ultra-Fast Phenomena V*, edited by G. R. Fleming and A. E. Siegman (Springer, Berlin, 1986), p. 303, and references therein.

[3]See the review by P. J. Rossky and J. Schnitker, J. Phys. Chem. **92**, 4277 (1988).

[4]B. J. Berne and D. Thirumalai, Annu. Rev. Phys. Chem. **37**, 401 (1986).

[5]*Electrons in Fluids*, edited by J. Jortner and N. R. Kestner (Springer, Heidelberg, 1973).

[6]A. Migus, Y. Gauduel, J. L. Martin, and A. Antonetti, Phys. Rev. Lett. **58**, 1559 (1987) and references therein.

[7]G. A. Kenney-Wallace and C. D. Jonah, J. Phys. Chem. **86**, 2572 (1982).

[8]J. M. Wiesenfeld and E. P. Ippen, Chem. Phys. Lett. **73**, 47 (1980).

[9]U. Landman, in *Computer Simulation Studies in Condensed Matter Physics*, edited by D. P. Landau, K. K. Mon, and H.-B. Schuttler (Springer, Heidelberg, 1988), p. 144; A. N. Barnett, V. Landman, D. Scharf, and J. Jortner, Acct. Chem. Res. (in press, 1989); J. Jortner, D. Scharf, and U. Landman in *Elemental and Molecular Cluster*, edited by G. Benedek, T. P. Martin, and G. Pacchioni (Springer, Berlin, 1988), p. 148.

[10]R. N. Barnett, U. Landman, and A. Nitzman, Phys. Rev. Lett. **62**, 106 (1989).

[11]D. Thirumalai, E. J. Bruskin, and B. J. Berne, J. Chem. Phys. **83**, 230 (1985).

[12]R. N. Barnett, U. Landman, and A. Nitzan, J. Chem. Phys. **89**, 2242 (1988) and references therein.

[13]R. N. Barnett, U. Landman, and A. Nitzan, J. Chem. Phys. **90**, 4413 (1989).

[14]A. Selloni, P. Carenvali, R. Car, and M. Parrinello, Phys. Rev. Lett. **59**, 823 (1987).

[15]J. Schnitker, K. Motakabbir, P. J. Rossky, and R. Friesner, Phys. Rev. Lett. **60**, 456 (1988).

[16]M. Sprik and M. L. Klein, J. Chem. Phys. **87**, 5987 (1987).

[17]J. Chang and W. H. Miller, J. Chem. Phys. **87**, 1648 (1987).

[18]J. D. Doll, R. D. Colson, and D. L. Freeman, J. Chem. Phys. **87**, 1641 (1987); J. D. Doll, Adv. Chem. Phys. (in press); J. D. Doll, D. L. Freeman, and M. J. Gillan, Chem. Phys. Lett. **143**, 277 (1988).

[19]A. L. Nichols III and D. Chandler, J. Chem. Phys. **87**, 6671 (1987).

[20]M. D. Feit, J. A. Feit, Jr., and A. Steiger, J. Comput. Phys. **47**, 412 (1982); M. D. Feit and J. A. Fleck, Jr., J. Chem. Phys. **78**, 301 (1983); **80**, 2578 (1984).

[21](a) D. Kosloff and R. Kosloff, J. Comput. Phys. **52**, 35 (1983); (b) R. Kosloff and H. Talezer, Chem. Phys. Lett. **127**, 223 (1986).

[22]See the review by R. Kosloff, J. Phys. Chem. **92**, 2087 (1988).

[23]Z. Kotler, A. Nitzan, and R. Kosloff, in *Tunneling*, edited by J. Jortner and B. Pullman (Reidel, Boston, 1986), p. 193.

[24]R. N. Barnett, U. Landman, C. L. Cleveland, and J. Jortner, J. Chem. Phys. **88**, 4421 (1988); **88**, 4429 (1988), and references therein.

[25]W. Weyl, Ann. Phys. **197**, 601 (1963); E. J. Hart and J. W. Boag, J. Am. Chem. Soc. **84**, 4090 (1962); *Solutions Metal-Ammoniac*, edited by G. Lepourtre and M. Sienko (Benjamin, New York, 1964); *Metal-Ammonia Solutions*, edited by J. J. Lagowski and M. Sienko (Butterworths, London, 1970); *Solvated Electrons*, edited by R. F. Gould, (American Chemical Society, Washington, D.C., 1965), Vol. 50; *Electron–Solvent and Anion–Solvent Interactions*, edited by L. Kevan and B. C. Webster (Elsevier, New York, 1976); E. J. Hart and M. Anbar, *The Hydrated Electron* (Wiley, New York, 1970); J. C. Thompson, *Electrons In Liquid Ammonia* (Clarendon, Oxford, 1976); U. Schindelwolf, Angew. Chem. Int. Ed. Engl. **17**, 887 (1978); B. C. Webster, Annu. Rep. Prog. Chem. Sec. C **76**, 287 (1979); D.-F. Feng and L. Kevan, Chem. Rev. **80**, 1 (1980); J. Jortner, Ber. Bunsenges. Phys. Chem. **75**, 646 (1971).

[26]M. Newton, J. Phys. Chem. **74**, 2795 (1975); D. Chipman, *ibid.* **83**, 1657 (1979); B. K. Rao and N. R. Kestner, J. Chem. Phys. **80**, 1587 (1984).

[27]M. Armbuster, H. Haberland, and H. G. Schindler, Phys. Rev. Lett. **47**, 323 (1981).

[28]H. Haberland, C. Ludewigt, H. G. Schindler, and D. R. Worsnop, Surf. Sci. **156**, 157 (1985).

[29]H. Haberland, H. Langosch, H. G. Schindler, and D. R. Worsnop, Ber. Bunsenges. Phys. Chem. **88**, 270 (1984).

[30]H. Haberland, H. G. Schindler, and D. R. Worsnop, J. Chem. Phys. **81**, 3742 (1984).

[31]J. V. Coe, D. R. Worsnop, and K. H. Bowen, J. Chem. Phys. **88**, 8014 (1988).

[32]M. Kanpp, O. Echt, D. Kreisle, and E. Recknagel, J. Chem. Phys. **85**, 636 (1986); J. Phys. Chem. **91**, 2601 (1987).

[33]A. Wallqvist, D. Thirumalai, and B. J. Berne, J. Chem. Phys. **85**, 1583 (1986).

[34]U. Landman, R. N. Barnett, C. L. Cleveland, D. Scharf, and J. Jortner, J. Phys. Chem. **91**, 4890 (1987).

[35]R. N. Barnett, U. Landman, C. L. Cleveland, and J. Jortner, Phys. Rev. Lett. **59**, 811 (1987).

[36]R. N. Barnett, U. Landman, C. L. Cleveland, N. R. Kestner, and J. Jortner, J. Chem. Phys. **88**, 6670 (1988); Chem. Phys. Lett. **148**, 249 (1988).

[37]R. N. Barnett, U. Landman, C. L. Cleveland, and J. Jortner, Chem. Phys. Lett. **145**, 382 (1988).

[38]R. N. Barnett, U. Landman, and A. Nitzan, Phys. Rev. A **38**, 2178 (1988).

[39]R. Kosloff and C. Cerjan, J. Chem. Phys. **81**, 3722 (1984).

[40]B. Carmeli and H. Metiu, Chem. Phys. Lett. **133**, 543 (1987).

[41]P. Pechukas, Phys. Rev. **181**, 174 (1969).

[42]A. D. Mclachlan, Mol. Phys. **7**, 139 (1964).

[43]D. Kumamoto and R. Silbey, J. Chem. Phys. **75**, 6164 (1981).

[44]G. A. Kenney-Wallace, Adv. Chem. Phys. **47**, 535 (1981); G. A. Kenney-Wallace, in *Picosecond Phenomena*, edited by C. V. Shank, E. P. Ippen,

and S. L. Shapiro (Springer, Berlin, 1978).

[45]J. Schnitker, P. J. Rossky, and G. A. Kenney-Wallace, J. Chem. Phys. **85**, 2986 (1986).

[46]K. A. Motakabbir and P. J. Rossky, Chem. Phys. **129**, 253 (1989).

[47]G. W. Robinson, P. J. Thistlethwaite, and J. Lee, J. Phys. Chem. **90**, 4224 (1986).

[48]C. E. Krohn, P. R. Antoniewicz, and J. C. Thompson, Surf. Sci. **101**, 241 (1980); G. T. Bennett and J. C. Thompson, J. Chem. Phys. **84**, 1901 (1986).

[49]P. M. Rentzepis, R. P. Jones, and J. Jortner, J. Chem. Phys. **59**, 766 (1973); Chem. Phys. Lett. **15**, 480 (1972).

[50]D. C. Walker, J. Phys. Chem. **84**, 1140 (1980).

[51]D. F. Callef and P. G. Wolynes, J. Chem. Phys. **78**, 4145 (1983).

[52]A. Hinchliffe, D. G. Bounds, M. L. Klein, I. R. McDonald, and R. Righini, J. Chem. Phys. **74**, 1211 (1981).

[53]G. Herzberg, *Infrared and Raman Spectra* (Van Nostrand Reinhold, New York, 1945), Table 43, p. 177.

[54]R. N. Barnett, U. Landman, and J. Jortner, J. Chem. Phys. (to be published).

[55]J. R. Reimers and P. O. Watts, Chem. Phys. **85**, 83 (1984); **64**, 95 (1982). See also Ref. 24.

[56]In this context, we note that for the ammonia clusters the interaction potential between the excess electron and the molecule (Ref. 36) yields results which are consistent with experimental observations for the ground state properties, (Ref. 36) while the values obtained for the excitation energies are too large in comparison with experiment (Ref. 25) [see Fig. 2(a)]. For the excess electron in water, however, both the ground state properties and the excitation energies are in satisfactory quantitative agreement with experiment (Refs. 9, 10, 24, 37, and 58). Consequently, in our discussion below of the dynamical evolution of the excitation spectrum (see Figs. 1 and 5), we focus on analysis of the excess electron in a water cluster system.

[57]J. Schnitker and P. J. Rossky, J. Chem. Phys. **86**, 3462, 3471 (1987).

[58]J. Jortner, U. Landman, and R. N. Barnett, Chem. Phys. Lett. **152**, 353 (1988).